Investigation of Direct Force Control For Aerocapture at Neptune

Rohan G. Deshmukh[a], David A. Spencer[b], Soumyo Dutta[c]

[a]*PhD Candidate, Purdue University, 480 W Stadium Ave., West Lafayette, IN, 47907, USA, deshmur@purdue.edu*
[b]*Associate Professor, Purdue University, 480 W Stadium Ave., West Lafayette, IN, 47907, USA, dspencer@purdue.edu*
[c]*Aerospace Engineer, NASA Langley Research Center, 1 NASA Dr., Hampton, VA, 23681, USA, soumyo.dutta@nasa.gov*

Abstract

In this work, a direct force control numerical predictor-corrector guidance architecture is developed to enable Neptune aerocapture using blunt body aeroshells. A linear aerodynamics model is formulated for a Mars Science Laboratory-derived aeroshell. The application of optimal control theory shows that the ΔV-minimizing angle of attack and side-slip angle control laws are bang-bang. A closed-loop numerical predictor-corrector direct force control guidance algorithm is developed and numerically simulated using the Program to Optimize Simulated Trajectories II. A series of Monte Carlo simulations are conducted to assess the guidance robustness to uncertainties in vehicle aerodynamics, atmospheric density, and entry state. For the reference set of uncertainties, the direct force control vehicle achieves 99.7% successful science orbit insertion within a 330 m/s total ΔV budget for periapsis raise, apoapsis, inclination, and ascending node corrections. Improved atmospheric knowledge and delivery state accuracy are shown to improve the success to 100% and reduce the ΔV to 230 m/s. Direct force control is demonstrated to be an enabling technology for blunt body aerocapture at Neptune while providing comparable performance to existing slender body vehicles studied in literature.

Keywords:
Aerocapture, Neptune, GN&C

1. Introduction

Missions to the Neptune system can enable fundamental science regarding the formation of the solar system. To date, Voyager 2 is the only spacecraft to approach the distant ice giant, with a 1979 flyby of Neptune at a closest approach altitude of 4,950 km. The design of an orbital mission at Neptune is challenging, due to the velocity change required for orbital insertion. As an example, for a hyperbolic inertial entry velocity of 29 km/s, the amount of dissipated orbital velocity needed for elliptical orbit insertion is about 5.5 km/s. Chemical propellant could be utilized to provide the necessary orbit insertion maneuver, but the propellant would constitute a significant amount of the mass of the flight system. Some studies have suggested that Neptune missions are enabled by aerocapture due to benefits in the payload delivered to orbit as compared to the best nonaerocapture alterative[1]. As a result, aerocapture has been recently envisioned as a preferred orbit insertion technique at Neptune.

Aerocapture is a mission concept envisioned for orbit insertion about planetary bodies that have substantial atmospheres. As illustrated in Figure 1, aerocapture utilizes a planetary atmosphere for orbital energy dissipation of a hyperbolic entry trajectory. During atmospheric flight, the vehicle is actively guided to ensure sufficient energy is dissipated and the desired orbit plane is achieved once atmospheric exit is reached. For a science mission, the desired science orbit can be parameterized by the periapsis radius, r_p^t, apoapsis radius, r_a^t, as well as orbit inclination, i^t, and longitude of ascending node, LAN^t. After exiting the atmosphere, a series of propulsive burns are conducted to raise periapsis out of the atmosphere and correct any residual errors in the orbit's apoapsis and orbit plane.

Neptune mission architectures employing aerocapture have been studied in literature. In 2005, the National Aeronautics and Space Administration (NASA) conducted an inter-center systems analysis of Neptune aerocapture to assess the feasibility, benefit and risk of an aerocapture system, and identify technology gaps and performance goals[2]. The analysis was centered around a Neptune-Triton exploration mission concept that targeted a nominal 3,896 x 430,000 km retrograde orbit to enable Triton observations. After a 10.25 year transit time using solar electric propulsion combined with gravity assists at Venus and Jupiter, aerocapture was studied as the orbit insertion technique for

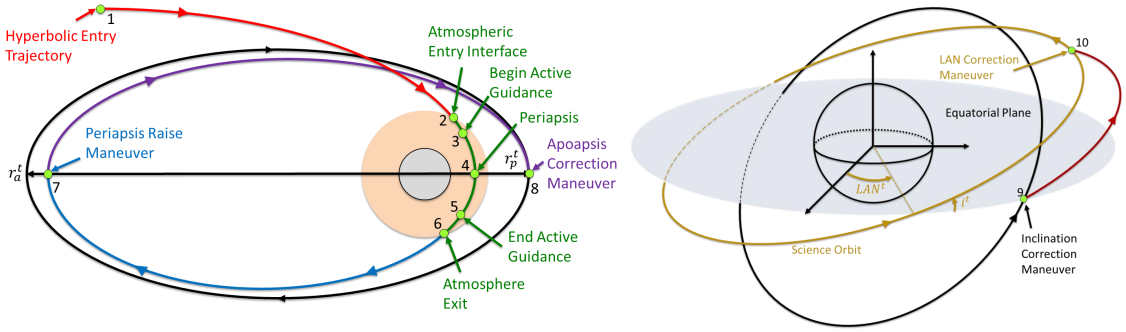

Figure 1: Aerocapture orbit insertion technique where planetary atmosphere is utilized to capture a hyperbolic entry trajectory into a desired science orbit. The left and right pictures denotes the in-plane and out-of-plane views of the aerocapture sequence, respectively. The sequence of events are denoted by the numbers. Four propulsive burns to correct periapsis and apoapsis radius, inclination, and longitude of ascending node represent the total orbit insertion cost.

capturing a 29 km/s entry hyperbola. The study concluded that aerocapture can enable a delivered mass-to-orbit that is 1.4 times greater than that for a chemical propulsive orbit insertion for the same launch vehicle. A critical architectural assumption utilized by the study was selecting a higher lift-to-drag ratio (L/D) slender body vehicles over a blunt body vehicle based on the need for a larger entry flight path angle corridor width[3]. Nevertheless, the study does not demonstrate why such a lower L/D blunt body vehicle cannot be utilized. A potential reason for this conclusion is the reliance on the bank angle flight control technique for the vehicle's guidance.

The study utilized the Hybrid Predictor-corrector Aerocapture Scheme (HYPAS) as the candidate aerocapture guidance algorithm. HYPAS has been analyzed extensively at other planetary destinations including Earth, Venus, Mars, and Titan [4]. The algorithm utilizes a combination of analytically derived equations and a reference drag and altitude profile for determining the bank angle commands. As a two-phase analytical predictor-corrector, the algorithm first balances the applied forces to achieve equilibrium glide then targets apoapsis once a specified velocity is reached in the trajectory [5]. Periodic bank reversals are conducted to manage the orbit plane. Monte Carlo simulation results of HYPAS for the Neptune aerocapture mission demonstrated sufficient orbit insertion performance and robustness to the simulated dispersions [6]. Moreover, the study did suggest that the stressful conditions of the Neptune mission warranted further investigations into advanced aerocapture guidance algorithms and the potential performance benefit using angle of attack modulation [7].

One such investigation is the formulation of a direct force control (DFC) numerical predictor-corrector (NPC) guidance algorithm. Utilizing a constant control variable, the NPC predicts the trajectory from the current vehicle state to atmospheric exit by numerically integrating the governing atmospheric flight equations of motion. Furthermore, the NPC utilizes numerical optimization methods to modify the control such that the orbit insertion error is minimized. Despite being more computationally expensive as compared to existing analytical guidance algorithms, NPC offers the highest level of accuracy in trajectory optimization. Recent advancement in space-rated flight computer computational power enable the applicability of on-board NPC algorithms. As a result, aerocapture NPC guidance algorithms have been investigated extensively in literature [8, 9]. DFC is a proposed and promising flight control methodology that utilizes the combination of angle of attack and side-slip angle for decoupling downrange and crossrange trajectory control. Unlike bank angle, the ability to modulate vehicle L/D during flight make DFC a potential enabler for blunt body Neptune aerocapture. Some literature exists in DFC for Entry, Descent, and Landing applications [10] but no literature exists in the application of DFC for planetary aerocapture.

In this work, a DFC aerocapture guidance architecture is developed to assess the feasibility and robustness of Neptune aerocapture using blunt body aeroshells. An analytical aerodynamics model for an aeroshell derived from the Mars Science Laboratory (MSL) design is utilized in the guidance formulation. ΔV-minimal flight control laws for angle of attack and side-slip angle are mathematically derived from the application of optimal control theory. The flight control laws are integrated into a closed-loop numerical predictor-corrector guidance architecture. A series of Monte Carlo simulations are conducted on a blunt body vehicle with two distinct angle of attack bounds to assess the performance and robustness of the designed DFC guidance. Results from assessing the effect of modifications to

Neptune's atmospheric dispersions and atmospheric delivery state uncertainity are presented.

2. Direct Force Control Guidance

DFC modulates the vehicle's angle of attack, α, and side-slip angle, β, in order to orient and control the magnitude of the aerodynamic lift, L, drag, D, and side force, Q, vectors. This is in contrast to BAM where the bank angle, σ, is modulated to rotate the lift vector about the freestream velocity vector. Figure 2 provides a visualization of the flight control distinction between DFC and BAM. Modulating α and β allows for full decomposition of the horizontal, side, and vertical motion with respect to the vehicle's principal x, y, and z axes.

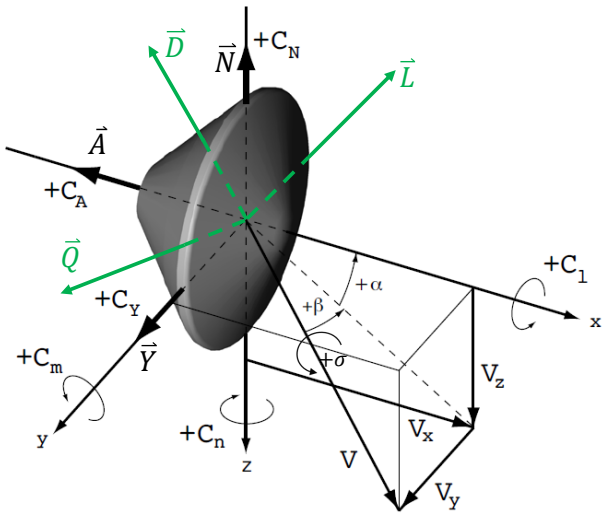

Figure 2: Visualization of aerodynamic forces, flight controls, and aerodynamic coefficents and moments present during aerocapture. Image adapted from Reference 11.

Figure 2 also illustrates an important distinction between body-frame, ($\vec{A}\ \vec{Y}\ \vec{N}$), and wind-frame, ($\vec{D}\ \vec{Q}\ \vec{L}$), aerodynamic forces, where A is the axial force, N is the normal force, and Y is the side force. Angle of attack and side-slip angle serve as Euler rotation angles between the two frames denoted by the transformation from body-frame aerodynamic force coefficients to wind-frame force coefficients in Eq. (1). The transformation is needed because the atmospheric flight equations of motion utilized in the guidance design utilize wind-frame aerodynamics while the vehicle's aerodynamic model is described in the body-frame.

$$\begin{bmatrix} C_D \\ C_Q \\ C_L \end{bmatrix} = \begin{bmatrix} \cos\alpha\cos\beta & -\sin\beta & \sin\alpha\cos\beta \\ \cos\alpha\sin\beta & \cos\beta & \sin\alpha\sin\beta \\ -\sin\alpha & 0 & \cos\alpha \end{bmatrix} \begin{bmatrix} C_A \\ C_Y \\ C_N \end{bmatrix} \tag{1}$$

2.1. Aerodynamics Model

An analytical aerodynamics model is sought to faciliate the formulation of the DFC flight control laws. This study utilizes the MSL aerodynamics database for modeling the hypersonic aerodynamics of a blunt body vehicle. The database contains a collection of hypersonic body-frame aerodynamic coefficient data computed using the Langley Aerothermal Upwind Relaxations Algorithm (LAURA) as functions of angle of attack, side-slip angle, and Mach number [12]. Although the database contains real-gas solutions for the Mars-based MSL flight regime, it provides a first-order model for obtaining analytical aerodynamics of a 70° sphere-cone blunt body. Querying the database and rotating the body-frame to the wind-frame using Eq. (1) yields non-linear expressions for the aerodynamic coefficients.

To achieve simplified analytical expressions, a first-order Taylor series approximation is made about zero angle of attack and side-slip angle along with assuming insignificant influence of Mach number. This linear approximation

results in L/D and side force coefficient shown by the dashed lines in Figure 3. The database solution is denoted by the solid lines in Figure 3. The vehicle L/D is primarily influenced by angle of attack while the vehicle side force coefficient is primarily influenced by side-slip angle. The contours demonstrate that the linearization sufficiently models the vehicle L/D for a large angle of attack range and sufficiently models side force coefficient for small side-slip angles. Up to ±30° angle of attack and ±5° side-slip angle, the linear model is within 10% of the database solution in L/D and C_Q. These corresponding values are assumed to be the upper acceptable limits of accuracy of the linear model and are quite valid for application on blunt bodies. Although the linear model simplifies the optimal control formulation, the small inaccuracies can potentially affect the robustness of the aerocapture trajectories. As a result, the linear model is rigorously tested against the full MSL database in the Monte Carlo simulations.

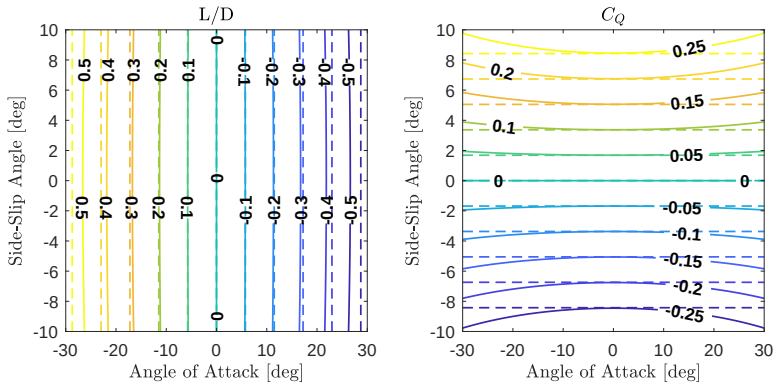

Figure 3: Comparison of vehicle L/D and side force coefficient, C_Q, vs angle of attack and side-slip angle between the linear aerodynamics model (dashed lines) and the MSL aerodynamics database (solid lines).

2.2. Guidance

The DFC guidance is formulated through the application of optimal control theory. The derivation follows a similar methodology as that presented in Reference 13 where the optimal aerocapture guidance for BAM is derived. However, the primary differences in the presented derivation are 1) the flight control method, 2) presence of side force in state dynamics, and 3) the vehicle platform.

For DFC, the guidance commands both angle of attack and side-slip angle such that the two-burn scheme for periapsis raise, ΔV_1, and apoapsis correction, ΔV_2, is minimized. This cost functional, $P = |\Delta V_1| + |\Delta V_2|$, is derived from two-body orbital mechanics as shown in Eq. (2) where μ is the gravitational constant of Neptune, r_a is the post-aerocapture apoapsis radius, a is the post-aerocapture semi-major axis, and r_p^t and r_a^t are the targeted periapsis and apoapsis radius. The post-aerocapture apoapsis radius and semi-major axis are defined by Eq. (3) and Eq. (4) using the inertial velocity magnitude, V_I, position vector magnitude, r, and flight path angle, γ_I, values at atmospheric exit.

$$P = \sqrt{2\mu}\left[\left|\sqrt{\frac{1}{r_a} - \frac{1}{r_a + r_p^t}} - \sqrt{\frac{1}{r_a} - \frac{1}{2a}}\right| + \left|\sqrt{\frac{1}{r_p^t} - \frac{1}{r_p^t + r_a^t}} - \sqrt{\frac{1}{r_p^t} - \frac{1}{r_a + r_p^t}}\right|\right] \tag{2}$$

$$a = \frac{\mu}{\frac{2\mu}{r} - {V_I}^2} \tag{3}$$

$$r_a = a\left[1 + \sqrt{1 - \frac{(V_I r \cos(\gamma_I))^2}{\mu a}}\right] \tag{4}$$

With the utilization of a two-burn scheme, the apoapsis radius boundary condition is not explicitly enforced. However, minimization of the cost functional can be achieved by minimizing the apoapsis correction burn. This occurs when the post-aerocapture and target apoapsis radii are equal. The orbit inclination at atmospheric exit is enforced as shown in Eq. (5) where $i(\vec{x}_{exit})$ is the post-aerocapture orbital inclination computed from the state vector

at atmospheric exit and i^t is the targeted inclination. The inclination is managed using separate lateral logic presented later in the paper.

$$i\left(\vec{x}_{exit}\right) - i^t = 0 \tag{5}$$

The aforementioned state vector is $\vec{x} = \begin{bmatrix} r & \theta & \phi & V & \gamma & \psi \end{bmatrix}^T$ with components corresponding to the radial distance, r, longitude, θ, geocentric latitude, ϕ, planet-relative velocity magnitude, V, flight path angle of the planet-relative velocity vector, γ, and heading angle of the planet-relative velocity vector, ψ, respectively. The corresponding state vector dynamics governing atmospheric flight in an ellipsoid rotating planet are derived in Reference 14 and are reproduced below in Eq. (6) – Eq. (11). The application of side-slip angle introduces side force, in addition to lift, into the flight path angle and heading angle dynamics. For DFC, zero bank angle is assumed to decouple the dynamics making lift only affect flight path angle and side force only affect heading angle.

$$\dot{r} = V \sin\gamma \tag{6}$$

$$\dot{\theta} = \frac{V \cos\gamma \sin\psi}{r \cos\phi} \tag{7}$$

$$\dot{\phi} = \frac{V \cos\gamma \cos\psi}{r} \tag{8}$$

$$\dot{V} = \frac{-D\left(\rho, V, \alpha\right)}{m} - g_r \sin\gamma - g_\phi \cos\gamma \cos\psi + \Omega^2 r \cos\phi \left(\sin\gamma \cos\phi - \cos\gamma \sin\phi \cos\psi\right) \tag{9}$$

$$\begin{aligned} \dot{\gamma} = \frac{1}{V}\Big[&\frac{L\left(\rho, V, \alpha\right)}{m} \cos\sigma + \frac{Q\left(\rho, V, \beta\right)}{m} \sin\sigma + \left(\frac{V^2}{r} - g_r\right)\cos\gamma + g_\phi \sin\gamma \cos\psi \\ &+2\Omega \mathrm{V} \cos\phi \sin\psi + \Omega^2 r \cos\phi \left(\cos\gamma \cos\phi + \sin\gamma \cos\psi \sin\phi\right)\Big] \end{aligned} \tag{10}$$

$$\begin{aligned} \dot{\psi} = \frac{1}{V}\Big[&\frac{L\left(\rho, V, \alpha\right) \sin\sigma}{m \cos\gamma} - \frac{Q\left(\rho, V, \beta\right) \cos\sigma}{m \cos\gamma} + \frac{V^2}{r} \cos\gamma \sin\psi \tan\phi + g_\phi \frac{\sin\psi}{\cos\gamma} \\ &+2\Omega \mathrm{V} \left(\tan\gamma \cos\psi \cos\phi - \sin\phi\right) + \frac{\Omega^2 r}{\cos\gamma} \sin\gamma \sin\phi \cos\phi\Big] \end{aligned} \tag{11}$$

Neptune dependent parameters influencing the state dynamics include the planetary gravity model, modeled by g_r and g_ϕ, rotation rate, Ω, and the atmosphere, modeled by ρ. Assuming the gravitational acceleration is dependent upon a radial term, g_r, latitudinal term, g_ϕ, and a gravitational potential up to the J_2 zonal term, the planetary gravity is modeled by Eq. (12) and Eq. (13) where R_e is Neptune's equatorial radius. Atmospheric density, ρ, is assumed to be a function of vehicle position and is computed using the Neptune Global Reference Atmospheric Model (NeptuneGRAM) [15].

$$g_r = \frac{\mu}{r^2}\left[1 + J_2\left(\frac{R_e}{r}\right)^2 \left(1.5 - 4.5\sin^2\phi\right)\right] \tag{12}$$

$$g_\phi = \frac{\mu}{r^2}\left[J_2\left(\frac{R_e}{r}\right)^2 \left(3 \sin\phi \cos\phi\right)\right] \tag{13}$$

The inertial velocity and flight path angle can be computed from the planet-relative state vector by the Eq. (14) and Eq. (15) as derived in Reference 16.

$$V_I = \sqrt{v^2 + 2\Omega r V \cos\gamma \cos\psi \cos\phi + \left(\Omega r \cos\phi\right)^2} \tag{14}$$

$$\tan\gamma_I = \frac{V \sin\gamma}{\sqrt{\left(V \cos\gamma\right)^2 + 2\Omega r V \cos\gamma \cos\psi \cos\phi + \left(\Omega r \cos\phi\right)^2}} \tag{15}$$

The aerodynamics utilized by the guidance comes from the derived blunt body linear aerodynamics model. With this approximate model and zero bank angle, angle of attack independently influences both flight path angle dynamics via lift modulation in Eq. (10) as well as the relative-velocity magnitude via drag modulation in Eq. (9) while side-slip angle independently influences heading angle dynamics via side force modulation in Eq. (11). The resulting independent control authority over the state dynamics will play an important role in the optimal control formulation.

2.3. Optimal Control

To obtain the optimal control laws for angle of attack and side-slip angle, the Euler-Lagrange equations from the calculus of variations solution to the optimal control problem is utilized [17]. The optimal aerocapture problem is a Mayer-type problem meaning the cost functional consists of only the terminal cost. This indicates the Lagrangian is zero. The first step is the definition of the Hamiltonian, H, which for a Mayer-type problem is defined by adjoining the co-state variables, λ_r, λ_θ, λ_ϕ, λ_V, λ_γ, and λ_ψ, to the state dynamics as shown in Eq. (16).

$$H = \lambda_r \dot{r} + \lambda_\theta \dot{\theta} + \lambda_\phi \dot{\phi} + \lambda_V \dot{V}(\alpha) + \lambda_\gamma \dot{\gamma}(\alpha) + \lambda_\psi \dot{\psi}(\beta) \tag{16}$$

For this application, the set of admissible angles of attack and side-slip angles are explicitly constrained by a minimum and maximum value as shown by Eq. (17) and Eq. (18). For an axisymmetric blunt body, both angles can be negatives.

$$\alpha_{min} \leq \alpha \leq \alpha_{max},\ \alpha_{min} \leq 0 \tag{17}$$

$$\beta_{min} \leq \beta \leq \beta_{max},\ \beta_{min} \leq 0 \tag{18}$$

Because of the control constraints, the full Euler-Lagrange equations cannot be explicitly utilized to obtain the optimal control laws. Rather, Pontryagin's minimum principle must be applied, which indicates that the Hamiltonian must be minimized with respect to the control vector. Eq. (16) along with Eq. (10) and Eq. (11) indicate that both angle of attack and side-slip angle are linear with respect to the Hamiltonian. As a result, the Hamiltonian can be written in the compact form $H = H_0 + H_1\alpha + H_2\beta$ where H_1 and H_2 are two switching functions defined by Eq. (19) and Eq. (20). In these two equations, m and S_{ref} are the vehicle's mass and aerodynamic reference area, C_{L_α} is the linear coefficient of lift slope, C_{D_α} is the linear coefficient of drag slope, and C_{Q_β} is the linear coefficient of side-force slope.

$$H_1 = \lambda_\gamma \left[\frac{1}{2m}\rho V S_{ref} C_{L_\alpha}\right] - \lambda_V \left[\frac{1}{2m}\rho V^2 S_{ref} C_{D_\alpha}\right] \tag{19}$$

$$H_2 = -\lambda_\psi \left[\frac{1}{2m\cos\gamma}\rho V S_{ref} C_{Q_\beta}\right] \tag{20}$$

Applying Pontryagin's minimum principle yields a bang-bang optimal control law for angle of attack, α^*, and side-slip angle, β^*, as described by Eq. (21) and Eq. (22). The cases in which either switching function equals zero for some finite time interval within the initial and final time is known as a singular arc. Using a similar proof-by-contradiction approach utilized in BAM optimal control, the singular arcs can be shown to not exist. Without loss of generality, the result below indicates that the optimal control structure for DFC aerocapture vehicles where linear aerodynamics are suitable is bang-bang and the parameter of optimization is the control switch time(s). It is important to keep in mind that the true non-linear aerodynamics model and the addition of flight control actuation constraints will cause the resulting flight control laws to be non-optimal but will be very close the theoretical optimum. Nonetheless, this a-priori knowledge of the ΔV-minimizing DFC flight control law is advantageous as it can be integrated into a NPC framework to serve as the on-board guidance.

$$\alpha^* = \begin{cases} \alpha_{min}, & \text{if } H_1 > 0 \\ \alpha_{max}, & \text{if } H_1 < 0 \\ \in [\alpha_{min}, \alpha_{max}], & \text{if } H_1 \equiv 0 \text{ in } [t_1, t_2] \subset \left[t_0, t_f\right] \end{cases} \tag{21}$$

$$\beta^* = \begin{cases} \beta_{min}, & \text{if } H_2 > 0 \\ \beta_{max}, & \text{if } H_2 < 0 \\ \in [\beta_{min}, \beta_{max}], & \text{if } H_2 \equiv 0 \text{ in } [t_3, t_4] \subset \left[t_0, t_f\right] \end{cases} \tag{22}$$

2.4. Numerical Predictor-Corrector

With the optimal control law structure known, the on-board trajectory optimization problem is solved utilizing a NPC framework. The existing Fully Numerical Predictor Aerocapture Guidance (FNPAG) presented in Reference 9, which is originally designed for BAM, is modified for DFC application. The algorithm consists of two phases during atmospheric flight as illustrated by Figure 4. First, the guidance hold occurs from atmospheric entry until the atmosphere is sensed, which is defined by a sensed g-load greater than 0.01. Once reached, the guidance activates and Phase 1 begins. During every guidance cycle in Phase 1, the guidance determines the angle of attack switch time that minimizes the two-burn ΔV using the golden-section method while flying at maximum angle of attack. Phase 1 ends once the optimized switch time is reached. At this point, the angle of attack switches and Phase 2 begins. During every guidance cycle in Phase 2, the guidance determines the constant angle of attack value within the imposed bounds that minimizes the two-burn ΔV until guidance shut off, occurring when sensed g-load is less than 0.01. This control optimization is done to mitigate trajectory dispersions caused by atmospheric density perturbations after Phase 1. After guidance shut off, the guidance is held until atmospheric exit. In summary, the NPC predicts the trajectory by integrating the equations of motion to atmospheric exit with the univariate design parameter, either switch time or angle of attack, and corrects the design parameter by utilizing the unconstrained and parameter-bounded golden-section optimization method.

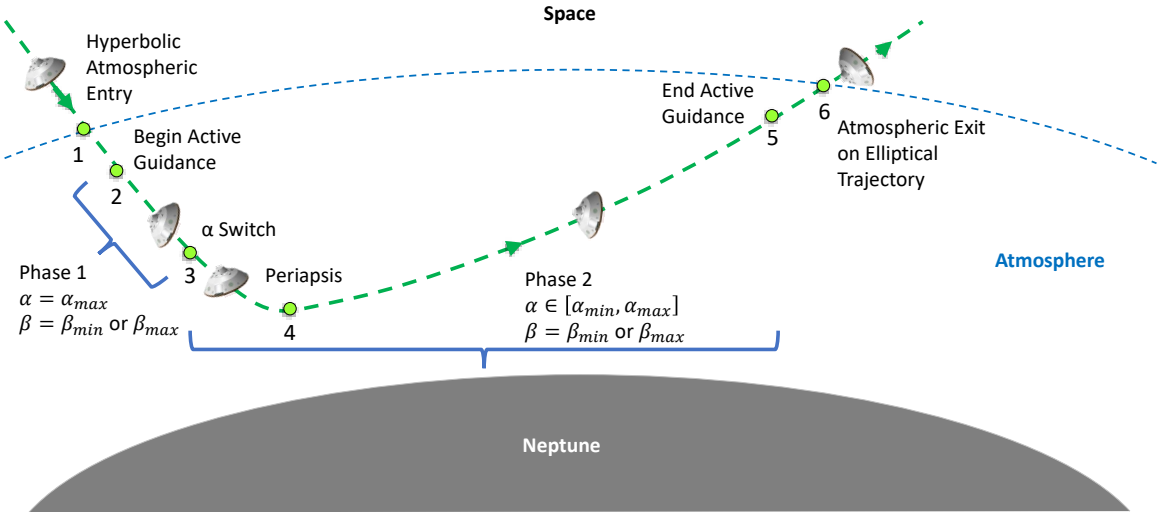

Figure 4: Two-phase direct force control Neptune aerocapture guidance.

The NPC optimization is unconstrained due to separate handling of the inclination constraint. For this separate handling, the bank angle reversal logic utilized in FNPAG is adapted to side-slip angle reversals. At guidance activation, the vehicle flies at a hold value, either maximum or minimum side-slip angle as shown in Figure 4. Using a predictive lateral logic that manages inclination error[18], side-slip angle reversals from each control bound are conducted. The number of reversals are prescribed and are utilized in the predictive logic. Although the corresponding side-slip angle switch time is not explicitly optimized, the side-slip angle lateral logic uses the fact that the derived side-slip angle control law presented in the previous section is bang-bang.

To improve the atmospheric density model utilized by the NPC in the presence of dispersions, an atmospheric estimator is utilized each guidance cycle. The estimator compares the sensed aerodynamic accelerations to nominal profile accelerations for determination of the density scale factors using a first-order fading memory filter. The vehicle inertial navigation system is assumed to have perfect state knowledge of the vehicle dynamics throughout

the trajectory. For actual flight applications, the perfect knowledge assumption would be replaced by the on-board measurements from the vehicle's inertial measurement unit and flush air data sensing system.

3. Experimental Setup

3.1. Numerical Simulation

For this study, a high-fidelity three degree-of-freedom truth simulation is utilized to assess the feasibility and performance of the designed DFC guidance architecture. The Programs to Optimize Simulated Trajectories II (POST2) is employed as the trajectory propagator[19]. An oblate gravity model with zonal harmonics up to J_2 is assumed. Atmospheric interface altitude is defined at 1000 km. The nominal atmopsheric profile from NeptuneGRAM is utilized by the NPC while atmopsheric perturbations about the nominal profile are simulated using the truth model. Although no active path constraints are enforced, the stagnation-point convective heat rate and integrated heat load are estimated using the Sutton-Graves relation for a reference nose radius of 1 m and Sutton-Graves coefficient of 6.79e-5 $kg^{0.5}/m$. The NPC utilizes the derived linear aerodynamics model while the truth utilizes the full non-linear MSL aerodynamics model with its internal dispersion model. The flight computer runs the guidance at 0.5 Hz. The angle of attack flight actuator is assumed to have rate and acceleration limits of 5 deg/s and 2 deg/s^2, respectively. Likewise, the side-slip angle flight actuator is assumed to have limits of 2 deg/s and 0.3 deg/s^2. Two control limit configurations for the blunt body are considered and are referred to as Scenario 1 and Scenario 2 for clarity. For Scenario 1, the angle of attack is bounded between ±20° while the side-slip angle is bounded between ±5°, resulting in a maximum L/D of 0.364. For Scenario 2, the angle of attack is bounded between ±30° while side-slip angle is bounded between ±5°, resulting in a maximum L/D of 0.578. The lateral logic is constrained to a maximum of three side-slip angle reversals.

The Neptune aerocapture mission assessed is identical to the one studied in the previous NASA Neptune aerocapture study found in Reference 2. The targeted retrograde elliptical orbit, with an apoapsis of 430,000 km periapsis of 3986 km, and orbit inclination of 153.547°, is designed to enable flybys of Triton. Although not explicitly targeted, the desired longitude of ascending node is 330.827°. The post-aerocapture four-burn ΔV scheme associated with periapsis raise, apoapsis correction, inclination correction, and ascending node correction are computed using POST2.

Figure 5 depicts a sample Scenario 2 numerical simulation results of the closed-loop DFC aerocapture guidance as applied to a nominal and dispersed Neptune atmospheric profiles. During Phase 2, the guidance commands modifications to angle of attack for mitigating the performance affects of the dispersions. These dispersions don't significantly affect the lateral logic side-slip angle reversals, which demonstrates the longitudinal and lateral motion decoupling capability of DFC.

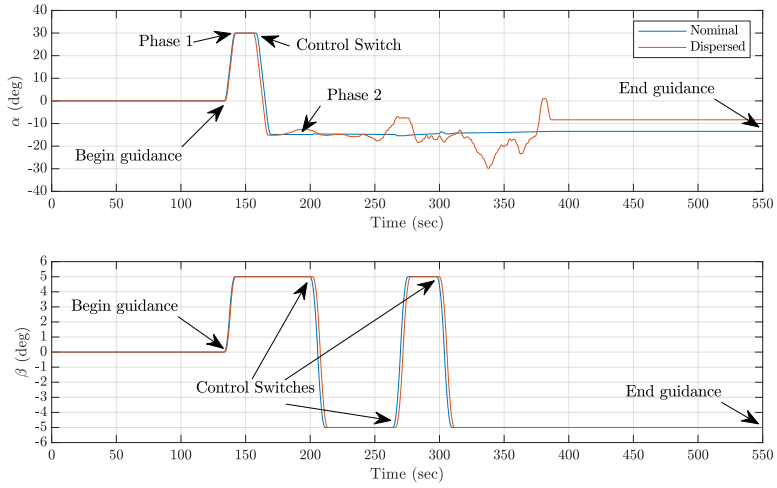

Figure 5: Sample Angle of Attack and Side Slip Angle commands from NPC guidance

3.2. *Monte Carlo Setup*

The Monte Carlo tests are conducted to assess the guidance algorithm robustness and statistical performance to a variety of simulated dispersions, including delivery state, atmospheric density, vehicle aerodynamics, and vehicle mass.

Table 1: Monte Carlo simulated dispersions for direct force control.

Category	Variable	Nominal	$\pm 3\sigma$ or min/max	Distribution
Delivery State	Inertial entry flight path angle	-12.3° or -12.5°	From covariance	Correlated
	B-plane angle	-176.500°	From covariance	Correlated
	Time of flight to entry interface	1.310 sec	From covariance	Correlated
	Inertial hyperbolic velocity	17.534 km/s	From covariance	Correlated
	V-infinity right ascension	-127.049°	From covariance	Correlated
	V-infinity declination	26.237°	From covariance	Correlated
Atmosphere	Random perturbation seed	1	1 to 29999	Uniform
	Fbias	0	-0.56 to 0.56	Uniform
	Fminmax	0	-1 to 1	Uniform
Aerodynamics	Lift coefficient	From MSL model	From MSL uncertanty	Normal
	Drag coefficient	From MSL model	From MSL uncertanty	Normal
	Side-force coefficient	From MSL model	From MSL uncertanty	Normal
Mass Properties	Weight	2200 kg	From MSL uncertanty	Normal

Table 2: Summary of Monte Carlo Test Cases.

Case	Perturbation Scale	Fminmax	Covariance Multiplier
1. Reference	1.0	f(latitude)	1.0
2. Reduced Density Perturbations	0.5	f(latitude)	1.0
3. Increased Density Perturbations	2.0	global	1.0
4. Reduced Delivery State Uncertanity	1.0	f(latitude)	0.5

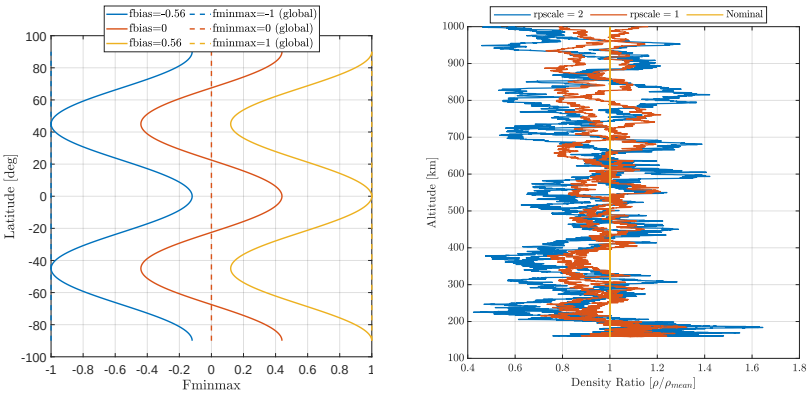

(a) Latitudinal variation of fminmax and global profiles

(b) Atmospheric density variations

Figure 6: Simulating atmospheric uncertanity using NeptuneGRAM

Table 1 lists the uncertainties and distribution types utilized in the 8001 individual Monte Carlo tests run with POST2. The full MSL aerodynamics model and its corresponding dispersions are simulated to rigorously test both the accuracy of the NPC linear aerodynamics model and subsequent performance of the guidance algorithm. Entry state dispersions are generated using similar correlated approach navigation performance from the previous NASA Neptune aerocapture study. In particular, the nominal inertial entry flight path angle is modified based off the theoretical corrdior width assessment. The entry flight path angle is set to -12.3° and -12.5° for Scenarios 1 and 2, respectively.

The knowledge of Neptune's atmosphere is a key driver in the feasibility and reliability of aerocapture. Neptune-GRAM is utilized to generate uniformly distributed dispersions in atmospheric density and simulate atmospheric wind perturbations. The atmospheric state can vary with altitude, latitude, season, and time of day. These variations are modeled in NeptuneGRAM using the term *fminmax*, which ranges between ±1. Modifying *fminmax* allows for a state vs altitude profile to be modeled for a particular latitude, season, and time of day. A similar Neptune arrival date as the previous NASA study is assumed. A similar sinusoidal latitudinal variation of *fminmax* is assumed using Eq. (23), where *fbias* is varied between ±0.56 to keep *fminmax* within its imposed bounds. Figure 6a depicts the sinusoidal latitudinal variation of *fminmax* for different *fbias* values.

$$fminmax = 0.44 \cos(4 * latitude) + fbias \tag{23}$$

Furthermore, random atmospheric variations are simulated using the parameter *rpscale* in NeptuneGRAM. This parameter scales the high frequency perturbations about the nominal atmospheric profile. A random perturbation seed is utilized in simulation of the random density variation. Figure 6b depicts sample density variations applied to a nominal density vs altitude profile for the inbound and outbound legs of the aerocapture trajectory. The plot suggests potentially ±60% density variation about the mean profile can occur.

Table 2 lists the different atmospheric dispersion cases applied in the Monte Carlo analysis. The reference case corresponds to a latitudinal variation of *fminmax* along with $\pm 3\sigma$ random density variations simulated. The second case corresponds to a 50% reduction in the random density variations. The third case corresponds to a removal of the latitudinal variation of *fminmax*, therby increasing the uncertainity in the mean density profile, as well as $\pm 6\sigma$ random density variations simulated. This case is intended to be representative of the worst-case scenario given the current knowledge of Neptune's atmosphere. The fourth case corresponds to a reduction in the delivery state uncertanity through a reduction in the covaraience matrix multiplier. The experimental setup for Cases 1 and 2 exactly match those found in Reference 6. Case 3 more rigorously simulates the effect of increased density uncertainty than that found in Reference 6 through doubling the perturbation scale. Case 4 represents an experimental setup not explored by Reference 6.

4. Results

4.1. Reference Case

For the reference case, Case 1, the reference set of uncertainties in Table 2 are utilized in the Monte Carlo analysis. The guidance actively minimizes the combination of periapsis raise and apoapsis correction manuevers by modulating angle of attack while the lateral logic maintains the orbit inclination by modulating side-slip angle. This is done in the presence of dispersions associated with delivery error, atmosphere, aerodynamics, and vehicle state. For Case 1, 95.7% and 99.7% of the simulated cases successfully captured into an elliptical orbit for Scenarios 1 and 2, respectively. The failed cases can be classified as either hyperbolic trajectories or trajectories that pass below the planet radius. Although not ideal, hyperbolic cases can be corrected through propulsive burns. Cases that pass within the planet radius cannot be corrected unless atmospheric "pop-up" burns, like those utilized in aerobraking, are integrated into the guidance logic. Nevertheless, the data suggests the trend that increasing the vehicle L/D capability can potentially enable 100% capture success.

For the successful cases in Case 1, Figure 7a shows the resulting aerocapture performance with regards to apoapsis altitude, orbit plane, peak g-load, and aeroheating. The apoapsis altitude vs periapsis altitude subplot shows Scenario 2 providing improved apoapsis targeting performance as compared to Scenario 1. By incorporating the periapsis raise maneuver into the cost functional, the guidance strives to keep the post-aerocapture periapsis altitude as large as possible. This provides a significant performance advantage over existing Neptune aerocapture guidance algorithm, which seeks to minimize the apoapsis altitude error only. This leads to potentially negative post-aerocapture periapsis altitudes that are propulsively expensive to raise out of the atmosphere. This observation can actually be seen in the Monte Carlo performance data found in Reference 6. Furthermore, Figure 7a shows the designed lateral logic using side-slip angle reversals is able to sufficiently to maintain orbit inclination to within $\pm 0.1^\circ$ while not significantly affecting ascending node for each scenario. The increase in vehicle L/D capability between Scenario 1 and 2 results in an increase in the peak g-load and peak heat rate while the converse leads to an increase in the integrated heat load. This may lead to potential trade-offs between orbit insertion performance and vehicle structural/thermal constraints.

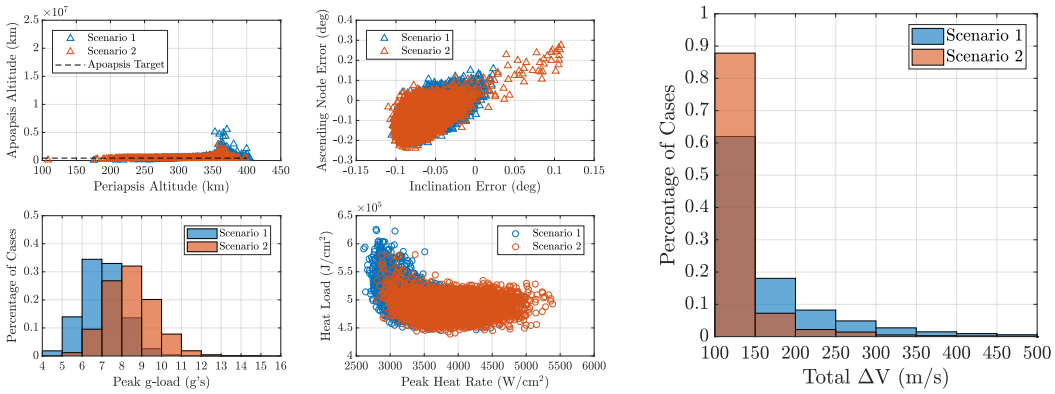

(a) Aerocapture Performance

(b) Orbit Insertion Total ΔV

Figure 7: Reference Case Monte Carlo Results

For the successful cases in Case 1, Figure 7b depicts the total ΔV histograms for each scenario. The ΔV constitute the sum of the post-aerocapture four-burns for periapsis raise, apoapsis correction, inclination correction, and ascending node correction. The results indicate that both vehicle configurations yield fuel efficient trajectories. But, the increased L/D capability of Scenario 2 leads to a majority of lower propulsive cost cases than Scenario 1.

The Monte Carlo orbit insertion performance statistics for the captured reference cases are shown in Table 3. The statisics from both scenarios show that the designed DFC guidance provides sufficient orbit insertion performance. The increase in L/D capability leads to a generous improvement in the apoapsis targeting and subsequent periapsis raise and apoapsis correction ΔV sum. The inclination error and subsequent orbit plane correction costs are sufficiently small. Despite having a minute inclination error, the inclination plus ascending node correction costs are noticeable. This is due to the precession of the ascending node due to Neptune planetary oblateness after the aerocapture sequence. This can be reduced by either conducting the ascending node correction earlier in the burn sequence or biasing the post-aerocapture ascending node. Due to this phenomena, most aerocapture scenarios utilize inclination as the preferred orbit plane performance metric.

Table 3: Reference Case Monte Carlo Statistics for direct force control aerocapture at Neptune.

Parameter	Mean	3σ	1^{st} percentile	50^{th} percentile	99^{th} percentile
Direct Force Control - Scenario 1					
Apoapsis Error, x10^3 km	52.084	603.057	-126.618	2.747	720.092
Inclination Error, deg	-0.049	0.059	-0.088	-0.050	-0.001
Periapsis + Apoapsis ΔV, m/s	142	320	83	106	490
Inclination + Node ΔV, m/s	29	8	23	29	35
Total ΔV, m/s	171	320	111	135	516
Direct Force Control - Scenario 2					
Apoapsis Error, x10^3 km	13.326	216.246	-51.723	0.656	241.224
Inclination Error, deg	-0.069	0.062	-0.097	-0.072	-0.009
Periapsis + Apoapsis ΔV, m/s	109	137	84	98	304
Inclination + Node ΔV, m/s	30	9	24	30	37
Total ΔV, m/s	138	138	112	128	333

4.2. Reduced Density Perturbations Case

For the reduced density perturbation case, Case 2, the density perturbation scale factor is reduced by half. This reduction might be possible with improved knowledge of Neptune's atmosphere say from preceding atmospheric entry probes. To assess its affect on the resulting Monte Carlo results, the parameter *rpscale* is modified from Case 1 Monte Carlo setup. For Case 2, 96.0% and 99.8% of the simulated cases succesfully captured for Scenario 1 and 2, respectively. This results in a small increase in the aerocapture success rate for each scenario as compared to Case 1.

Figure 8a shows the aerocapture performance metrics for Case 2. As compared to Case 1, Case 2 simulation yields improved apoapsis targeting cases for both vehicle scenarios but not significant changes in the orbit plane performance, peak g-load, and aeroheating metrics. Figure 8b shows the total ΔV for each scenario. As compared to Case 1, there is a noticeable improvement in the histograms. The reduction in density perturbation leads to a significant reduction in the high ΔV cost cases. This has a more profound effect on Scenario 1 results thereby illustrating the effect of improved atmospheric knowledge on enhancing the performance of lower L/D capability vehicles.

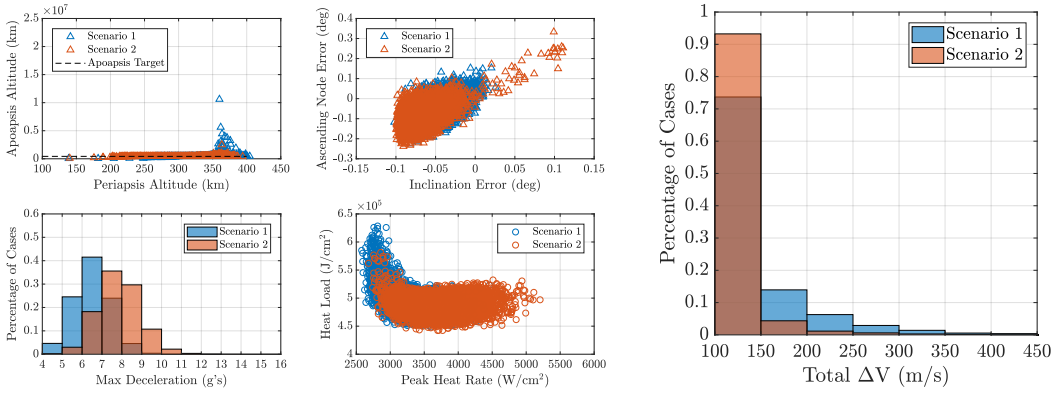

(a) Aerocapture Performance

(b) Orbit Insertion Total ΔV

Figure 8: Reduced Density Perturbations Case Aerocapture Performance

The Monte Carlo orbit insertion performance statistics for Case 2 are shown in Table 4. The reduced density perturbations signficantly reduces the 99th percentile apoapsis error and subsequently the corresponding apoapsis correction ΔV cost for both scenarios as compared to Case 1.

Table 4: Reduced Density Perturbations Monte Carlo Statistics for direct force control aerocapture at Neptune.

Parameter	Mean	3σ	1^{st} percentile	50^{th} percentile	99^{th} percentile
Direct Force Control - Scenario 1					
Apoapsis Error, x10^3 km	34.626	560.510	-79.920	0.714	378.018
Inclination Error, deg	-0.049	0.058	-0.087	-0.049	-0.002
Periapsis + Apoapsis ΔV, m/s	125	263	83	99	395
Inclination + Node ΔV, m/s	29	8	23	29	35
Total ΔV, m/s	153	263	111	129	422
Direct Force Control - Scenario 2					
Apoapsis Error, x10^3 km	7.528	122.388	-18.876	0.167	156.518
Inclination Error, deg	-0.068	0.058	-0.095	-0.071	-0.015
Periapsis + Apoapsis ΔV, m/s	103	153	84	98	232
Inclination + Node ΔV, m/s	30	8	24	30	37
Total ΔV, m/s	133	155	112	128	259

4.3. Increased Density Perturbations Case

For the increased density perturbation case, Case 3, the density perturbation scale factor is doubled and the latitudinal variation of *fminmax* is removed and replaced with a constant value for *fminmax* that can range between ±1. This case is meant to assess the largest possible density perturbation capability of NeptuneGRAM. For Case 3, 86.6% and 97.9% of the simulated cases succesfully captured for Scenario 1 and 2, respectively. This results in a noticeable decrease in the aerocapture success rate for each scenario as compared to Case 1. Figure 9a shows the aerocapture performance metrics for Case 3. As compared to Case 1, the increased case simulation degrades apoapsis targeting performance for both vehicle scenarios but does not significantly affect orbit plane performance. The peak g-load and peak heat rate increase as a result of the increased perturbations. Figure 9b shows the total ΔV for each scenario for Case 3. As compared to Case 1, there is a noticeable difference in the histograms. The increase in density perturbation

leads to a significant increase in the high ΔV cost cases for both scenarios. This indicates the vehicle has saturated its control authority over handling the incurred trajectory dispersions. With the increased L/D capability, Scenario 2 is able to produce more lower ΔV cost cases than Scenario 1. This trend indicates that enhanced performance can be obtained through further increases in vehicle L/D capability.

The Monte Carlo orbit insertion performance statistics for Case 3 are shown in Table 5. The increased density perturbations are shown to signficantly impact the 99th percentile apoapsis error and subsequently the corresponding apoapsis correction ΔV cost for both scenarios as compared to the reference case.

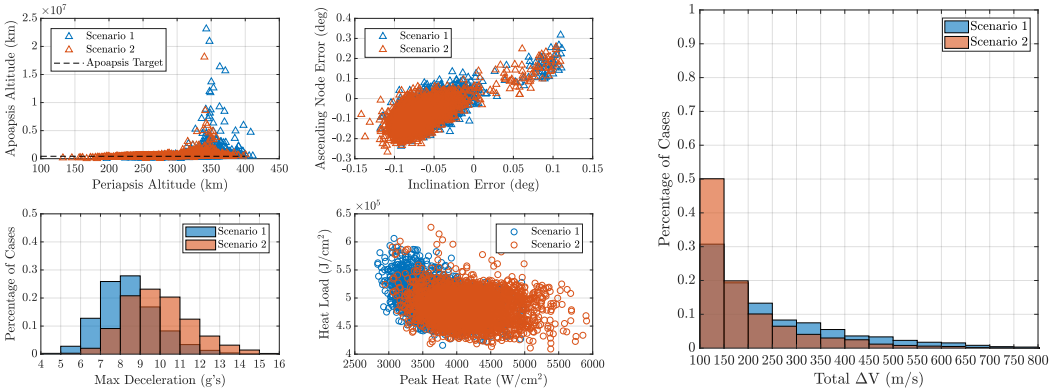

(a) Aerocapture Performance

(b) Orbit Insertion Total ΔV

Figure 9: Increased Density Perturbations Case Aerocapture Performance

Table 5: Increased Density Perturbations Monte Carlo Statistics for direct force control aerocapture at Neptune.

Parameter	Mean	3σ	1^{st} percentile	50^{th} percentile	99^{th} percentile
Direct Force Control - Scenario 1					
Apoapsis Error, x10^3 km	210.075	330.426	-235.703	5.136	4119.126
Inclination Error, deg	-0.051	0.088	-0.096	-0.055	0.089
Periapsis + Apoapsis ΔV, m/s	231	564	84	172	820
Inclination + Node ΔV, m/s	29	9	22	28	37
Total ΔV, m/s	259	567	112	200	857
Direct Force Control - Scenario 2					
Apoapsis Error, x10^3 km	86.129	1485.985	-177.603	2.278	1342.302
Inclination Error, deg	-0.067	0.086	-0.108	-0.073	0.076
Periapsis + Apoapsis ΔV, m/s	173	577	85	120	599
Inclination + Node ΔV, m/s	29	11	23	29	39
Total ΔV, m/s	202	581	113	150	626

4.4. Reduced Delivery State Uncertainty

For the reduced delivery state uncertainity case, Case 4, the same applied dispersions as Case 1 are applied except for the delivery state. The delivery state covariance matrix is reduced by a half. This may be possible due to improvements in the radiometric data and optical nagivation systems utilized by the mission. An example of such an enhancing technology might be the utilization of the Long Range Reconaissance Image Camera that was flown on the New Horizons spacecraft. Case 1 utilizes a delivery state covariance that corellates to an inertial entry flight path angle uncertainty of ±0.51°. From Reference 7, the previous NASA study utilized a 0.8 L/D slender aeroshell that enabled a theoretical entry flight path angle corridor width of 1.78°, which is much wider than the entry flight angle uncertainty. Using a similar approach, the theoretical corridor width for Scenario 1 and 2 are 0.35° and 0.98°, respectively. In the current form, Scenario 1 does not have a entry flight path angle corridor width wide enough to fully handle the

entry flight path angle uncertainty while Scenario 2 is barely wide enough. This is an inherent limitation of utilizing DFC on a blunt body vehicle. Nevertheless, a reduction in the uncertainty can potentially be advantageous for such a vehicle configuration.

For Case 4, 99.8% and 100% of the simulated cases succesfully captured for Scenario 1 and 2, respectively. This results in a significant increase in the aerocapture success rate for each scenario as compared to Case 1. Figure 10a shows the aerocapture performance metrics for Case 4. As compared to Case 1, the reduced delivery state case simulation doesn't significantly impact the apoapsis targeting performance nor the orbit plane performance for both vehicle scenarios. The peak peak heat rate and integrated heat load decrease while the peak g-load remains relatively the same due to the reductions in navigation uncertainty. Figure 10b shows the total ΔV for each scenario. As compared to Case 1, there is a slight improvement in the histograms. The reduced navigation errors reduce the number of high ΔV cost cases for both scenarios.

The Monte Carlo orbit insertion performance statistics for Case 4 are shown in Table 6. The reduced navigation errors are shown to noticeably reduce the 99th percentile apoapsis error and subsequently the corresponding apoapsis correction ΔV cost for both scenarios as compared to Case 1.

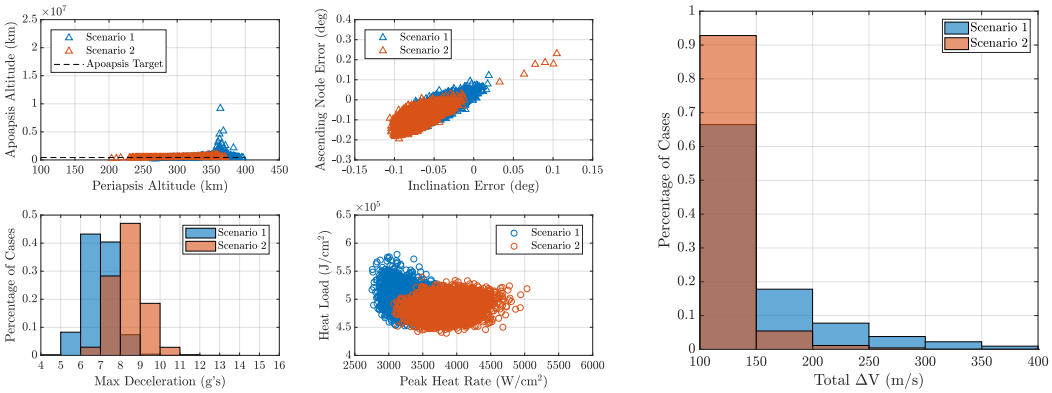

(a) Aerocapture Performance

(b) Orbit Insertion Total ΔV

Figure 10: Reduced Delivery State Uncertainty Case Aerocapture Performance

Table 6: Reduced Delivery State Uncertainty Monte Carlo Statistics for direct force control aerocapture at Neptune.

Parameter	Mean	3σ	1^{st} percentile	50^{th} percentile	99^{th} percentile
Direct Force Control - Scenario 1					
Apoapsis Error, x10^3 km	45.983	530.018	-55.846	3.074	505.657
Inclination Error, deg	-0.049	0.050	-0.084	-0.049	-0.007
Periapsis + Apoapsis ΔV, m/s	130	185	83	103	374
Inclination + Node ΔV, m/s	29	5	25	29	32
Total ΔV, m/s	158	183	112	132	399
Direct Force Control - Scenario 2					
Apoapsis Error, x10^3 km	7.725	83.547	-17.007	0.617	121.476
Inclination Error, deg	-0.070	0.044	-0.096	-0.072	-0.032
Periapsis + Apoapsis ΔV, m/s	102	63	84	98	192
Inclination + Node ΔV, m/s	30	4	26	30	33
Total ΔV, m/s	131	62	113	127	222

5. Conclusion

The application of a direct force control guidance for planetary aerocapture at Neptune is investigated in this work. The investigation included the formulation of an analytical aerodynamics model for a blunt body aeroshell as well as the application of optimal control theory for developing flight control laws for angle of attack and side-slip

angle modulation. It is found that the ΔV minimizing flight controls for angle of attack and side-slip angle have a bang-bang structure. This finding faciliated the application of a two-phase closed-loop numerical predictor-corrector guidance algorithm, which utilizes angle of attack for in-plane ΔV minimization and side-slip angle for orbit plane management. Blunt-body aerocapture employing direct force control with two different angle of attack modulation capabilities are investigated for elliptical orbit insertion about Neptune. A series of Monte Carlo numerical simulations are conducted to assess the DFC guidance performance and robustness to delivery state, atmospheric, aerodynamic, and mass dispersions. Overall, the simulation results validate the application of a linear aerodynamics model for facilitating the derivation of fuel-minimizing flight control laws for DFC

The performance analysis has shown for the reference set of uncertanities, DFC can enable a 99.7% successful science orbit insertion within a 330 m/s total ΔV budget for periapsis raise, apoapsis, inclination, and ascending node corrections. For the same reference set, Reference 6 demonstrated with a slender 0.8 L/D aeroshell employing BAM 100% successful science orbit insertion within a 360 m/s ΔV budget for periapsis raise and apoapsis correction burns only. For a significantly larger set of atmospheric dispersions, DFC can enable a 97.9% succesful science orbit insertion within a 630 m/s total ΔV budget. The two vehicle configurations analyzed suggest that increasing the vehicle L/D through larger angle of attack modulation range can both improve the orbit insertion and reduce the ΔV. If better knowledge of Neptune's atmosphere leads to a 50% reduction in the density uncertainties, then DFC can enable a 99.8% succesful science orbit insertion within a 260 m/s total ΔV budget. For this same set, Reference 6 demonstrated 100% successful science orbit insertion within a 270 m/s ΔV budget for periapsis raise and apoapsis correction burns only. If improved navigation model leads to a 50% reduction in the delivery state covariance, then DFC can enable a 100% succesful science orbit insertion within a 230 m/s total ΔV budget.

The results presented for DFC demonstrates the relevance of the flight control technique as an enabling and enhancing aerocapture technology. DFC is demonstrated to enable blunt body Neptune aerocapture. Despite having a lower L/D capability, DFC enables aerocapture performance and robustness comparable to an alternative flight control method that utilize BAM on a mid-L/D slender body. The numerical simulation studies conducted demonstrate that DFC aerocapture risk can be further reduced through improvements in delivery state accuracy and knowledge of the planetary atmosphere. DFC technology itself is enabled by advancements in hypersonic flight control actuator technology. With investments in this field and others addressed, DFC has the potential to augment aerocapture performance both at Neptune and at other planetary destinations.

Acknowledgments

The authors would like to acknowledge Dr. Ping Lu for providing the framework for FNPAG.

Funding Source

This research was conducted at National Aeronautics and Space Administration Langley Research Center under the NASA Internship, Fellowships & Scholarships Program.

References

[1] J. Hall, M. Noca, R. Bailey, Cost-benefit analysis of the aerocapture mission set, Journal of Spacecraft and Rockets 42 (2) (2005) 309–320.

[2] M. K. Lockwood, K. T. Edquist, B. R. Starr, B. R. Hollis, G. A. Hrinda, R. W. Bailey, J. L. Hall, T. R. Spilker, M. A. Noca, N. O. Kongo, R. J. Haw, C. G. Justus, A. L. Duvall, V. W. Keller, K. Sutton, R. E. Dyke, Aerocapture Systems Analysis for a Neptune Mission, Technical Memorandum NASA/TM-2006-214300, National Aeronautics and Space Administration (April 2006).

[3] M. K. Lockwood, Neptune Aerocapture Systems Analysis, in: AIAA Atmospheric Flight Mechanics Conference and Exhibit, AIAA, Providence, RI, 2004. doi:AIAA 2004-4951.

[4] J. Masciarelli, Aerocapture Guidance Algorithm Development and Testing, in: 2007 NASA Science Technology Conference, University of Maryland University College, 2007. doi:NSTC2007.

[5] C. Cerimele, J. Gamble, A simplified guidance algorithm for lifting aeroassist orbital transfer vehicles, in: AIAA 23rd Aerospace Sciences Meeting, Reno, NV, 1985. doi:AIAA 85-0348.

[6] B. Starr, C. Westhelle, J. Masciarelli, Aerocapture Performance Analysis for a Neptune-Triton Exploration Mission, in: AIAA Atmospheric Flight Mechanics Conference and Exhibit, Providence, RI, 2004. doi:AIAA 2004-4955.

[7] J. Masciarelli, C. H. Westhelle, C. A. Graves, Aerocapture Guidance Performance for the Neptune Orbiter, in: AIAA Atmospheric Flight Mechanics Conference and Exhibit, Providence, RI, 2004. doi:AIAA 2004-4954.

[8] R. W. Powell, Numerical Roll Reversal Aerocapture and Precision Landing Guidance Algorithms for the Mars Surveyor Program 2001 Missions, in: AIAA Atmospheric Flight Mechanics Conference, Boston, MA, 1998. doi:AIAA 1998-4574.
[9] K. D. Webb, P. Lu, A. M. Dwyer Cianciolo, Aerocapture Guidance for a Human Mars Mission, in: AIAA Guidance, Navigation, and Control Conference in AIAA SciTech Forum, Grapevine, TX, 2017. doi:AIAA 2017-1900.
[10] A. Cianciolo, R. Powell, Entry, descent, and landing guidance and control approaches to satisfy mars human mission landing criteria, Vol. 160, Univelt Inc., 2017, pp. 1397–1410.
[11] M. Schoenenberger, F. M. Cheatwood, P. Desai, Static Aerodynamics of the Mars Exploration Rover Entry Capsule, in: 43rd AIAA Aerospace Sciences Meeting and Exhibit, Reno, NV, 2005. doi:AIAA 2005-56.
[12] A. Dyakonov, M. Schoenenberger, J. Van Norman, Hypersonic and Supersonic Static Aerodynamics of Mars Science Laboratory Entry Vehicle, in: 43rd AIAA Thermophysics Conference, New Orleans, LA, 2012. doi:AIAA 2012-2999.
[13] P. Lu, C. J. Cerimele, M. A. Tigges, D. A. Matz, Optimal Aerocapture Guidance, Journal of Guidance, Control, and Dynamics 38 (4) (2015) 553–565.
[14] N. Vinh, A. Busemann, R. Culp, Hypersonic and planetary entry flight mechanics, University of Michigan Press, Ann Arbor, MI, 1980.
[15] C. G. Justus, A. Duval, V. W. Keller, Atmospheric Models for Aerocapture Systems Studies, in: AIAA Atmospheric Flight Mechanics Conference and Exhibit, Providence, RI, 2004. doi:AIAA 2004-3844.
[16] A. Miele, Z. G. Zhao, W. Y. Lee, Optimal trajectories for the Aeroassisted Flight Experiment. Part 1: Equations of motion in an Earth-fixed system, Contractor Report NASA-CR-186134, Rice University (1989).
[17] J. Longuski, G. J.J., P. J.E., Optimal Control with Aerospace Applications, 1st Edition, Space Technology Library ; 32, Springer New York : Imprint: Springer, 2014.
[18] K. M. Smith, Predictive Lateral Logic for Numerical Entry Guidance Algorithms, in: 26th AAS/AIAA Space Flight Mechanics Meeting, Napa, CA, 2016. doi:AAS 16-216.
[19] S. Striepe, R. Powell, P. Desai, E. Queen, D. W. Way, J. L. Prince, A. Cianciolo, J. Davis, D. Litton, R. Maddock, J. Shidner, R. Winski, S. O'Keefe, A. Bowes, J. Aguirre, C. Garrison, J. Hoffman, A. Olds, S. Dutta, C. Zumwalt, J. White, G. Brauer, S. Marsh, R. Lugo, J. Green, M. Engel, Program To Optimize Simulated Trajectories (POST II), Vol. II Utilization Manual, NASA Langley Research Center, Hampton, VA, 4th Edition (November 2017).